First-principles calculations of electronic structure and optical and elastic properties of the novel ABX₃-type LaWN₃ perovskite structure†

Xing Liu,[ab] Jia Fu [ID] *[a] and Guangming Chen [ID] [c]

The development of ABX₃-type advanced perovskite materials has become a focus for both scientific researchers and the material genome initiative (MGI). In addition to the traditional perovskite ABO₃ and halide perovskite ABX₃, LaWN₃ is discovered as a new ABX₃-type advanced perovskite structure. The elastic and optical properties of this novel LaWN₃ structure are systematically studied *via* DFT. Based on the calculated elastic constants, the bulk modulus, shear modulus, Young's modulus and Pugh modulus ratio are precisely obtained. Results show that (1) LaWN₃ is an indirect bandgap semiconductor with a hybrid occuring near the Fermi level and the main contributions are La-d, W-d and N-p. (2) LaWN₃ has a certain ductility. The optical constants, such as absorption spectrum, energy-loss spectrum, conductivity, dielectric function, reflectivity and refractive index, are analyzed and the static dielectric constant is 10.98 and the refractivity index is 3.31. (3) The optical constants of LaWN₃ are higher than those of other existing ABX₃-type materials, showing very promising application as a functional perovskite in the future. The existence of this stable LaWN₃ structure might widen the perovskite material's application, such as in photodetectors, light-emitting diodes, perovskite solar cells, fuel cells and so on.

1 Introduction

The ABX₃-type advanced perovskite materials have become a research hotspot in recent years, including the traditional perovskite ABO₃, organic–inorganic hybrid perovskite MAPbX₃ (X = Cl, Br, and I), halide perovskite ABX₃ (X = Cl, Br, and I). In recent years, perovskite materials ABX₃, with their special structural characteristics, have been widely used in the fields of catalysis,[1,2] piezoelectricity,[3–5] solar cells,[6,7] giant magnetoresistance,[8–10] and light-emitting diode materials[11–13] due to their unique physical structures. They have excellent physical–chemical properties, ferroelectric performance, ferromagnetic performance, superconductivity and fluorescence laser performance. The designed anisotropic single crystal at nano-scale as the instinct link helps to predict physical properties of larger structure at micro-scale and might be used to verify the isotropic properties of experimental phase using both experiment and simulation techniques.[14] These basic investigation

results can be applied in efficient solar modules coated by large-area perovskite films[15] and organic solar cells.[16]

The traditional perovskite ABO₃, organic–inorganic hybrid perovskite MAPbX₃ (X = Cl, Br, I) and halide perovskite ABX₃ (X = Cl, Br, I)[17] have been studied in theory and experiment. Liu *et al.*[18] synthesized CH₃NH₃PbBr₃ quantum dots with a tunable spectrum. The emission peak range is from green-blue to deep purple (523.6 nm and 432.9 nm, separately), which is wider than quantum dots made without changing the halide composition; thus the blue shift mechanism of the photoluminescence spectrum of CH₃NH₃PbBr₃ quantum dots is clear. Su *et al.*[19] realized a room temperature polarized laser in an experiment based on non-epitaxial all inorganic cesium lead perovskite microcavities. The polarized lasing is characterized by macroscopic ground state occupation, narrow linewidth and long-range spatial coherence accumulation. This significant work shows that the lead halide perovskites and doped perovskites have great application prospects in low cost, large area, high performance room temperature transistors or polarized light devices.[20–22] Today, the maximum efficiency of crystalline silicon cells has exceeded 26% (its limiting efficiency is 29%)[23] and the maximum efficiency of perovskite cells is higher than that of crystalline silicon cells. (The designed cell can theoretically reach an efficiency limit of 33% and the theoretical conversion limit of stacked cells is 43%.)[24,25] Although the perovskite battery has a high energy-saving limit, simple process, rapid

[a]*Shaanxi Key Laboratory of Material Processing Engineering, School of Material Science and Engineering, Xi'an Shiyou University, Xi'an, 710065, China. E-mail: fujia@xsyu.edu.cn*

[b]*State Key Laboratory of Solidification Processing, School of Materials Science and Engineering, Northwestern Polytechnical University, Xi'an 710072, PR China*

[c]*Shenzhen Key Laboratory of Polymer Science and Technology, College of Materials Science and Engineering, Shenzhen University, Shenzhen, 518060, China*

† Electronic supplementary information (ESI) available. See DOI: 10.1039/c9ra10735e

development, and impressive performance in the laboratory, there is still a long way to go for large-scale practical application.

For numerical simulation of ABX_3 structures, Wang *et al.*[26] found that ordered porous $La_{0.6}Sr_{0.4}MnO_3$ perovskite arrays are decomposed into hexagonal mesoporous nanoparticles, thus revealing a new crystal plane that is more active in the catalytic combustion of methane. The first-principles calculations show that fractures at the weak joints of the 3DOM structure provide a large area of (001) plane surface, which indicates that the energy barrier of hydrogen extraction is reduced, thus promoting methane oxidation. Based on DFT calculations, Lu *et al.*[27] found that there are three in-plane Fe states from different micro mechanisms, which revealed a new physical mechanism of 2D ferroelectricity in perovskite oxide films. Ryan *et al.*[28] screened about 2145 different perovskite compositions for potential application as SOFC cathodes with high activity and stability and verified that the screening method qualitatively reproduced the stability and conductivity of the cathode materials. Lanthanide ions can improve perovskite film properties due to their unique photophysical properties, such as long excited state life, long wavelength emission in the near infrared or visible region, and linear emission band.[29,30] With this background, $LaWN_3$ perovskite material is found as a new ABX_3-type advanced perovskite structure. The above published works focus on perovskite oxide (ABO_3) or inorganic–organic halide perovskites ($MAPbX_3$), while few studies have been found on the potential $LaWN_3$ structure. For this newly discovered $LaWN_3$ perovskite structure, the thermodynamic stability, mechanical stability and structural stability are studied and determined using the relevant theories of phonon dispersion,[31] elastic constants,[32] and tolerance factors,[33,34] respectively.

Reviewing previous studies, their investigations of perovskites in experiment and theory have made great achievements; however, as a new ABX_3-type material with perovskite structure, $LaWN_3$ has been rarely studied. So far, we are one of the few research groups to find this substance, apart from Hiroki Moriwake's group in the Nanostructures Research Laboratory of the Japan Fine Ceramics Center (JFCC),[35] and our group has systematically studied and confirmed that this stable structure has excellent comprehensive performance. The $LaWN_3$ perovskite material is a new ABX_3-type advanced perovskite structure. Therefore, the electronic structure, elasticity and optics of $LaWN_3$ are studied using the first-principles method. This paper aims to study the $LaWN_3$ electronic structure and optical and elastic properties based on DFT, which can provide theoretical parameters for experimentation and explore the significant value for applications of the designed perovskite with $LaWN_3$ structure.

2 Modelling and computational details

The ionic radius matching in perovskite structure should fit the following relationship

$$t = \frac{R_A + R_X}{\sqrt{2}(R_B + R_X)} \qquad (1)$$

where, R_A, R_B and R_x are the ionic radii of sites A, B and X.

The tolerance factor of perovskite allows a variety of elements to meet the structural requirements, so the materials show good elemental adjustability. Generally, A-site elements play a supporting role in perovskite structure, B-site elements are catalytic active sites, and there is mutual influence and restriction between A-site and B-site. The charge balance is also a factor for structural stability. Theoretically, if the radii of A, B and X ions meet the structural tolerance factor $0.81 < t < 1.11$, the typical perovskite crystal structure can exist stably.

For the $LaWN_3$ structure, the ionic radii of La and W and N are $R_{La} = 1.36$ Å, $R_W = 0.66$ Å and $R_N = 1.46$ Å, respectively. The tolerance factor is calculated as $t_{LaWN_3} = \dfrac{1.36 + 1.46}{\sqrt{2}(0.66 + 1.46)} = 0.941$ and the value of 0.941 is within the stability region of 0.81–1.11,[33] showing that the structure of $LaWN_3$ is relatively stable.

2.1 Structure model

Fig. 1 shows the crystal structure of $LaWN_3$. As can be seen from Fig. 1, $LaWN_3$ can be seen as a WN_6 octahedron connected at the top of the three-dimensional common angle. The A-site ions are located in the centre of the gap surrounded by BX_6 octahedra. The lattice constants are $a = b = 5.71$ Å, $c = 13.96$ Å, $\alpha = \beta = 90°$, and $\gamma = 120°$ (hexagonal type), the density is 9.2122 g cm^{-3} and the space group is $R3c$ with an H-lattice type.

2.2 Methods of calculations

The generalized gradient approximation (GGA) of Perdew–Burke–Ernzerhof functional is used to calculate the band structure and optical and elastic properties of $LaWN_3$ in this work.[36] The Cambridge Sequential Total Energy Package (CASTEP) is selected for calculation.[37,38] The plane wave function is expanded from the base plane. An ultrasoft pseudopotential is adopted to describe the interaction between electrons and ions, as it helps to reduce the number of base planes in convergence calculations and save computational resources. The function forms of GGA and PBE are selected to be exchange correlation functions. In the $LaWN_3$ structure, the La $5p^6 5d^1 6s^2$ electrons, W $5d^4 6s^2$ electrons, and N $2s^2 2p^3$ electrons are explicitly treated as valence electrons. The cut-off energy of the plane wave is taken as $E_{cut} = 300$ eV and Brillouin zone
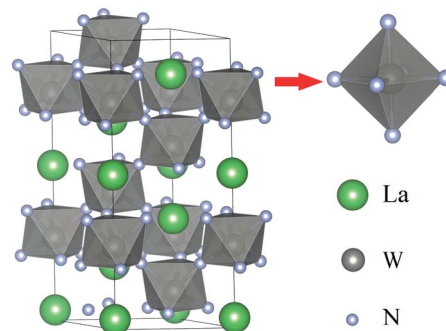

Fig. 1 Crystal structure of $LaWN_3$. The gray octahedron is WN_6.

integration is performed over $3 \times 3 \times 2$ grids using the Monkhorst–Pack method. The convergence thresholds for total energy, maximum force, maximum stress, maximum displacement and Hellmann–Feynman ionic force are respectively less than 5×10^{-7} eV per atom, 0.01 eV Å^{-1}, 0.02 GPa, 5.0×10^{-4} Å and 1 meV Å^{-1}.

3 Results and discussion

3.1 Geometry optimization

Geometric optimization is essential for the theoretical study of this new ABX$_3$-type LaWN$_3$ material. The calculation parameters are optimized in order to find the stable state and the ground state. As LaWN$_3$ research is rare, it is difficult to compare the optimization results with literature results. Therefore, different functional methods are used to optimize structural parameters of LaWN$_3$, with the error less than 2% between the two nearest optimizations. That is to say, the structural model with the most unchanged parameters is the structure in the ground state.

The stability of a crystal structure is related to its cohesive energy and formation heat, where the cohesive energy is often defined as the minimum work which is needed to decompose the crystal into single atoms. Generally, the larger the cohesive energy or the larger the negative value of the formation heat during the process of formation from its elements in exothermic reaction, the more stable the crystal structure is.[39]

The cohesive energy (E_{coh}) of a given phase is a measure of the strength of the forces which bind the atoms together in the solid state. The cohesive energy (E_{coh}) can be calculated by the standard relation[40,41]

$$E_{coh}^{AB} = E_{atom}^{A} + E_{atom}^{B} - E_{total}^{AB} \qquad (2)$$

where E_{total}^{AB} is the total energy of the compound (LaN, WN$_2$ and LaWN$_3$) with equilibrium lattice constants and E_{atom}^{A} and E_{atom}^{B} are the atomic energies of the pure constituents.

Hence, by eqn (2), the cohesive energies of LaN, WN$_2$ and LaWN$_3$ are calculated to be -16.674 eV per atom, -18.331 eV per atom and -20.526 eV per atom, respectively. The formation enthalpy should be considered the energy per atom of the pure constituents (LaN and WN$_2$) in their solid states. The formation enthalpy is determined to be about -14.4795 eV per f.u., which is lower than the result of Fang.[35]

Table 1 shows the structural parameters of the optimized LaWN$_3$ structure calculated with different functional methods (GGA–PBE, GGA–PBESOL and GGA–PW91). It can be seen that the lattice constants of LaWN$_3$ changed very little, with the relative error between lattice parameters within only 1%. Thus, we can infer that LaWN$_3$ reaches a stable state and further research into related properties can be performed.

3.2 Electronic structure

The solid energy band theory is used to determine the energy levels of electrons in solids, that is, energy bands can explain many basic physical properties of solids.[42,43]

As seen in Fig. 2, the bottom of the conduction band is not the same as the top of the valence band, so LaWN$_3$ is an indirect band gap semiconductor.[35] The bandgap is calculated to be 1.181 eV.

The density of states analysis is in Fig. 3; the whole DOS is divided into five parts, of which part I–part IV are mainly concentrated on the valence band, while part V appears in the conduction band. The low valence band (I) is mainly composed of W-s, with a bandwidth of 3.11 eV. The W-p and La-s orbitals contribute to part II, with a small amount of N-s contributing. Part III of the DOS has two peaks composed of the hybrid of L-p and N-s orbitals from -17.7 eV to -11.3 eV. On the left side of the Fermi level, part IV contains obvious hybridizations near the top of the valence band, with three elements (N-2p, La-5d, and W-5d orbitals) mainly contributing. For the conduction band region of part V, the orbitals of La-5d, W-5d and N-2p participate in the hybridization, thus forming a weak hybrid peak.

3.3 Phonon dispersion and molecular-orbital bonding

The stability of the perovskite material is key to its design and simulation. The phonon spectrum is closely related to the thermodynamic stability and can be used to verify an existing phase rather than a mesophase, which is beneficial to subsequent research and application in laboratory synthesis.[44]

Phonon spectra represent the collective vibration modes of the atoms that make up the material. If the primitive cell of the material contains n atoms, the phonon spectrum has a total of
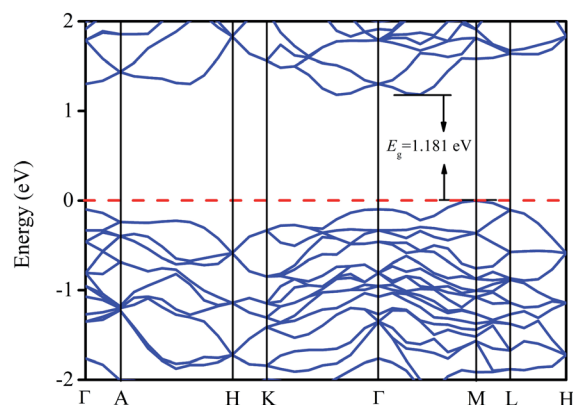
Table 1 Comparison of structural parameters calculated with GGA (PBE, PBESOL, CA-PZ) and LDA (PW91) methods. Lattice parameters a, b, c are in Å; α, β, γ are in degrees

	GGA		
Structural parameters	PBE	PBESOL	PW91
a	5.7363	5.7080	5.7368
b	5.7363	5.7080	5.7368
c	14.0038	14.0349	13.9985
α	90	90	90
β	90	90	90
γ	120	120	120

Fig. 2 Energy band of LaWN$_3$ structure; red dotted line indicates Fermi energy level.
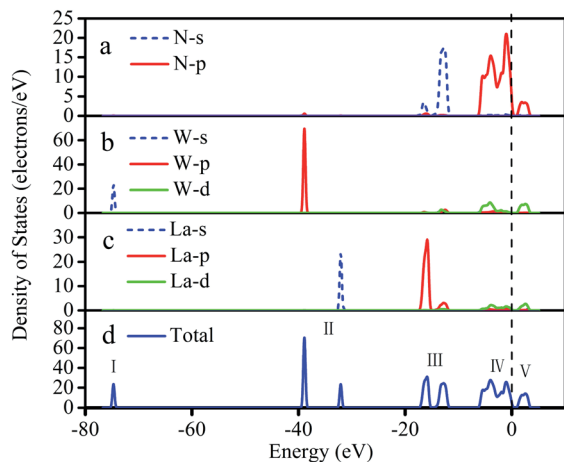
Fig. 3 DOS of LaWN$_3$ structure; black dotted line indicates Fermi energy level.

Fig. 4 The (a) phonon dispersion curves and (b) transverse & longitudinal waves in optics and acoustics of the $R3c$ LaWN$_3$ structure.

$3n$ branches, including 3 acoustic branches and $3n - 3$ optical branches. The acoustic branch represents the overall vibration of the cell and the optical branch represents the relative vibrations of the atoms in the cell.[45–48] The vibration frequency is described as

$$\omega = \sqrt{\frac{\beta}{m}} = \sqrt{\frac{1}{m} \frac{\partial^2 E(x)}{\partial x^2}} \quad (3)$$

where ω is the vibration frequency, β can be understood as an elastic constant, $E(x)$ is the interaction energy between atoms, x is the displacement of atoms from the equilibrium position, and m is the mass of atoms. Here, ω is a virtual frequency. When $\frac{\partial^2 E(x)}{\partial x^2} < 0$, that is to say, when the atomic equilibrium position is located at the "mountain top" of energy (similar to the parabolic vertex), the atoms in this equilibrium position are obviously unstable.

The relationship between the direction of atom displacement and the direction of lattice wave propagation should be considered in a three-dimensional lattice. If q moves along a symmetry axis of the crystal and the crystal rotates around this axis by $\pi/2$ (or $\pi/3$, $2\pi/3$) in a symmetry operation, the lattice wave can be divided into a transverse wave and a longitudinal wave. The atomic displacement of the transverse wave is perpendicular to the propagation direction of the wave and contains two degenerate frequency waves. The phonon dispersion diagram for LaWN$_3$ is shown in Fig. 4.

As in Fig. 4(a), there are five atoms in a cell of LaWN$_3$, with 15 dispersion curves, 3 acoustic branches and 12 optical branches. The frequencies of the acoustic branches are lower than that of the optical branch, so the three acoustic branches degenerate to G (shown by the red ring), and the 12 optical branches have multiple splits (shown by the green ring). The calculated phonon spectra have no imaginary frequency, which indicates that LaWN$_3$ is stable thermodynamically.

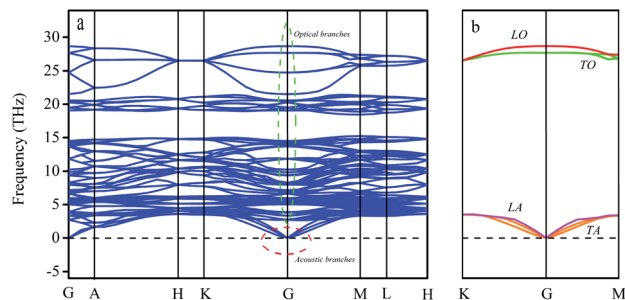To clarify the relationship between the transverse and longitudinal waves, the phonon dispersion diagram is simplified, as seen in Fig. 4(b). It can be seen that there are four coloured curves, the longitudinal optical branch (LO), transverse optical branch (TO), longitudinal acoustic branch (LA) and transverse acoustic branch (TA). The transverse waves (TO and TA) are composed by wave degeneracy of the same frequency (shown by the green and orange curves).

The molecular-orbital bonding of LaWN$_3$ structure is shown in Fig. 5. Based on the theories of crystal-field and molecular-orbital bonding,[49,50] the d-orbits of transition elements can be split in electrostatic fields with different symmetries. In LaWN$_3$, the d-orbit of the W atom would be split and two crystal field split levels would be formed in the On field, which are E$_g$ (d$_{x^2-y^2}$, d$_{z^2}$) and T$_{2g}$ (d$_{xy}$, d$_{xz}$, d$_{yz}$). A molecular orbital bonding diagram derived from the character of the states is presented in Fig. 5 to examine the chemical bonding of LaWN$_3$. With an increase of energy, N-2s and E$_g$, $\sigma 2$ p$_z$ and T$_{1u}$, $\pi 2$ (p$_x$ + p$_y$) and T$_{1u}$, $\sigma 2$ p$_z$ and E$_g$, $\pi 2$ (p$_x$ + p$_y$) and T$_{2g}$ respectively, contribute to the bonding from the bottom to the E_f. The corresponding antibondings are presented in Fig. 5 from the E_f to the top.

3.4 Homogenized elastic moduli of LaWN$_3$ structure

3.4.1 Elastic properties based on Reuss–Voigt–Hill method. Elasticity is not only related to mechanical stability, but is also closely related to Debye temperature, specific heat, wave velocity and other physical property parameters.[51–53] For
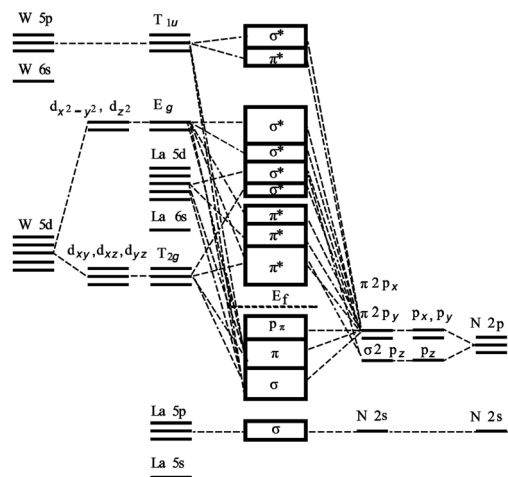

Fig. 5 Molecular–orbital bonding of LaWN$_3$.

hexagonal $LaWN_3$, there are six independent elastic constants (C_{11}, C_{33}, C_{44}, C_{12}, C_{13} and C_{66}). Due to the lack of comparable elastic constants for $LaWN_3$, other functional materials ($CaCO_3$, cubic-$SrZrO_3$ and α-$SrZrO_3$) are calculated to compare with previous calculation results to judge the correctness of calculation methods used.[54,55] The elastic constants of the relative crystal structures are listed in Table 2.

From Table 2, the elastic constants of other ABX_3 functional materials calculated by *ab initio* method are very close to those from previous works, showing that the calculation accuracy and DFT method are reasonable. Thus, we can safely say that the obtained elastic constants of $LaWN_3$ are precise. Elastic moduli are important parameters that reflect the extent of a solid's resistance to both elastic and plastic deformation, using various simulation techniques.[56]

Mechanical stability is commonly based on Born's stability restrictions, which are as follows.[57]

$$C_{44} > 0, \ C_{11} > |C_{12}|, \ (C_{11} > 2C_{12})C_{33} > 2C_{13}^2 \tag{4}$$

As the elastic constants satisfy Born's stability restrictions, we can infer that $LaWN_3$ is mechanically stable.

Bulk modulus and shear modulus are two parameters critical for describing the ability of a material to resist volume change and change of shape caused by shear force and bond angle, respectively. The bulk modulus and shear modulus can be obtained based on C_{ij}. There exist two limit bounds: one is from Reuss and can calculate the grain boundary strain continuity; the other is the grain boundary stress continuity proposed by Voigt. Hill proves that the calculations of the Reuss and Voigt models are the upper and lower limits of the elastic constant, respectively. The expressions of homogenized elastic moduli can be calculated as follows:

$$B_V = \frac{1}{9}[2(C_{11} + C_{12}) + 4C_{13} + C_{33}] \tag{5}$$

$$G_V = \frac{1}{30}(M + 12C_{44} + 12C_{66}) \tag{6}$$

$$B_R = \frac{C^2}{M} = \frac{(C_{11} + C_{12})C_{33} - 2C_{13}^2}{C_{11} + C_{12} + 2C_{33} - 4C_{13}} \tag{7}$$

$$G_R = \frac{5}{2} \times \frac{C^2 C_{44} C_{66}}{3B_V C_{44} C_{66} + C^2(C_{44} + C_{66})} \tag{8}$$

where, $M = C_{11} + C_{12} + 2C_{33} - 4C_{13}$ and $C^2 = (C_{11} + C_{12})C_{33} - 2C_{13}^2$.

The Young's modulus E of a material can be expressed as

$$E = 9B_x G_x/(G_x + 3B_x) \tag{9}$$

where, x = the Reuss, Voigt and Hill models.

The comparison of elastic moduli and available theoretical data for typical ABX_3 functional materials is listed in Table 3. For $LaWN_3$, the Young's modulus E_H is smaller than in other functional materials.[58–65] In our calculation of B_x/G_x, the Pugh values of $LaWN_3$ are higher than the critical value of 1.75 proposed by Pugh,[66] showing a certain ductility in $LaWN_3$.

3.4.2 Elastic properties based on Y-parameter method. Based on the definition of Reuss bounds, the Y-parameters normal to hexagonal crystal surface ($n = (u, v, w)$) are calculated by[60]

$$E_Y(u, v, w) = \frac{1}{S_{11} - [2(S_{11} - S_{13}) - S_{44}]w^2 + (S_{11} - 2S_{13} + S_{33} - S_{44})w^4} \tag{10}$$

$$G_Y(u, v, w) = \frac{1}{(2S_{11} - S_{12} - S_{13}) - (5S_{11} - S_{12} - 5S_{13} + S_{33} - 3S_{44})w^2 + 3(S_{11} - 2S_{13} + S_{33} - S_{44})w^4} \tag{11}$$

Table 2 Calculated independent elastic constants of $LaWN_3$ and available theoretical data for other materials

	Our work						Previous work		
	$LaWN_3$			$CaCO_3$	$SrZrO_3$	α-$SrZrO_3$	$CaCO_3$	$SrZrO_3$	α-$SrZrO_3$
	PBE	PW91	PBESOL	PBE	PBE	PBE	PBE	PBE	PBE
C_{11}	320.36	324.55	328.23	147.2	365.27	283.54	149.4	368.3	288.6
C_{22}	—	—	—	—	—	286.89	—	—	284.6
C_{33}	268.94	273.19	262.15	87.6		301.87	85.3	—	305.9
C_{12}	134.61	135.70	139.81	56.1	72.69	128.32	57.9	77.3	131.5
C_{13}	80.30	83.17	81.95	55.3	—	104.96	53.5	—	102.5
C_{23}	—	—	—	—	—	87.47	—	—	91.4
C_{44}	44.13	50.37	44.47	33.7	77.52	91.96	34.1	76.6	95.6
C_{55}	—	—	—	—	—	82.89	—	—	86.2
C_{66}	92.88	94.43	94.21	47.8	—	103.47	45.75	—	105

Table 3 Calculated bulk modulus, shear modulus, Young's modulus and Pugh ratios of other typical ABX_3 functional materials

	B		G		Young's moduli			Pugh		
	B_V	B_R	G_V	G_R	E_V	E_R	E_H	B_V/G_V	B_R/G_R	B_H/G_H
$LaWN_3$(PBE)	166.68	162.97	77.19	65.80	200.6	173.98	187.39	2.16	2.48	2.31
$LaWN_3$(PW91)	169.60	166.04	80.38	71.45	208.25	187.46	197.90	2.11	2.32	2.21
$LaWN_3$(PBESOL)	169.56	164.42	77.62	66.21	202.04	175.13	188.67	2.18	2.48	2.32
$SmAlO_3$ (ref. 58)	194.42	194.42	148.96	148.19	134.71	120.91	107.12	1.31	1.31	1.31
$SmCoO_3$ (ref. 59)	204.63	204.63	137.57	124.52	337.16	310.57	323.98	1.49	1.64	1.56
$CaCO_3$ (ref. 60–62)	76	69.63	36	28.71	93.27	75.72	84.56	2.11	2.43	2.25
	89.78	83.84	39.17	37.49	102.59	97.88	100.24	2.29	2.24	2.26
	77.81	71.55	36.72	35.08	95.19	90.46	92.83	2.12	2.04	2.08
$SrZrO_3$ (ref. 63–65)	160.2	160.2	99.72	92.75	247.75	233.24	240.54	1.61	1.73	1.66
	192.83	192.83	97.94	91.08	251.28	236.07	243.71	1.97	2.12	2.04
	147.64	147.64	92.19	89.31	228.92	222.97	225.95	1.60	1.65	1.63

where w is the normal direction cosine of the hexagonal crystal surface.

Similarly, for the Voigt bounds of hexagonal polycrystals, the Y-parameter containing the surface normal can be described as follows.[60]

$$E_Y(u, v, w) = \{[C_{11} + C_{12} + C_{13} - w^2(C_{11} + C_{12} - C_{13} - C_{33})]$$
$$[2C_{11} - C_{12} - C_{13} - w^2(5C_{11} - C_{12} - 5C_{13} + C_{33} - 12C_{44}) + 3w^4(C_{11} - 2C_{13} + C_{33} - 4C_{44})]\}/\{2C_{11} + C_{12} + C_{13} - w^2(3C_{11} + C_{12} - 3C_{13} - 4C_{44}) + w^4(C_{11} - 2C_{13} + C_{33} - 4C_{44})\} \quad (12)$$

$$G_Y(u, v, w) = \frac{1}{4}[2C_{11} - C_{12} - C_{13} - w^2(5C_{11} - C_{12} - 5C_{13} + C_{33} - 12C_{44}) + 3w^4(C_{11} - 2C_{13} + C_{33} - 4C_{44})] \quad (13)$$

Based on the elastic compliance, the Young's modulus E_Φ and shear modulus G_Φ in either direction of the hexagonal crystal making an angle Φ with the c-axis can be described as[67]

$$\frac{1}{E_\phi} = S_{11}(1 - l_3^2)^2 + S_{33}l_3^4 + (2S_{13} + S_{44})l_3^2(1 - l_3^2) \quad (14)$$

$$\frac{1}{G_\phi} = S_{44} + \left(S_{11} - S_{12} - \frac{S_{44}}{2}\right)(1 - l_3^2) + 2(S_{11} + S_{33} - 2S_{13} - S_{44})l_3^2(1 - l_3^2)^2 \quad (15)$$

where $l_3 = \cos\theta$ is the cosine of the normal orientation L_3 within the crystal plane and S_{ij} is the compliance coefficient.

For a hexagonal structure, the relationships between elastic stiffness C_{ij} and elastic compliance S_{ij} are as follows.[67]

$$S_{11} - S_{12} = (C_{11} - C_{12})^{-1} \quad (16)$$

$$S_{11} + S_{12} = C_{33}/[C_{33}(C_{11} + C_{12}) - 2C_{13}^2] \quad (17)$$

$$S_{13} = -C_{13}/[C_{33}(C_{11} + C_{12}) - 2C_{13}^2] \quad (18)$$

$$S_{33} = (C_{11} + C_{12})/[C_{33}(C_{11} + C_{12}) - 2C_{13}^2] \quad (19)$$

$$S_{44} = C_{44}^{-1} \quad (20)$$

From eqn (10)–(13) and eqn (14)–(20), the elastic moduli of hexagonal $LaWN_3$ can be calculated using the Y-parameter. The elastic moduli based on the Y-parameter can then be determined by the Reuss and Voigt models.
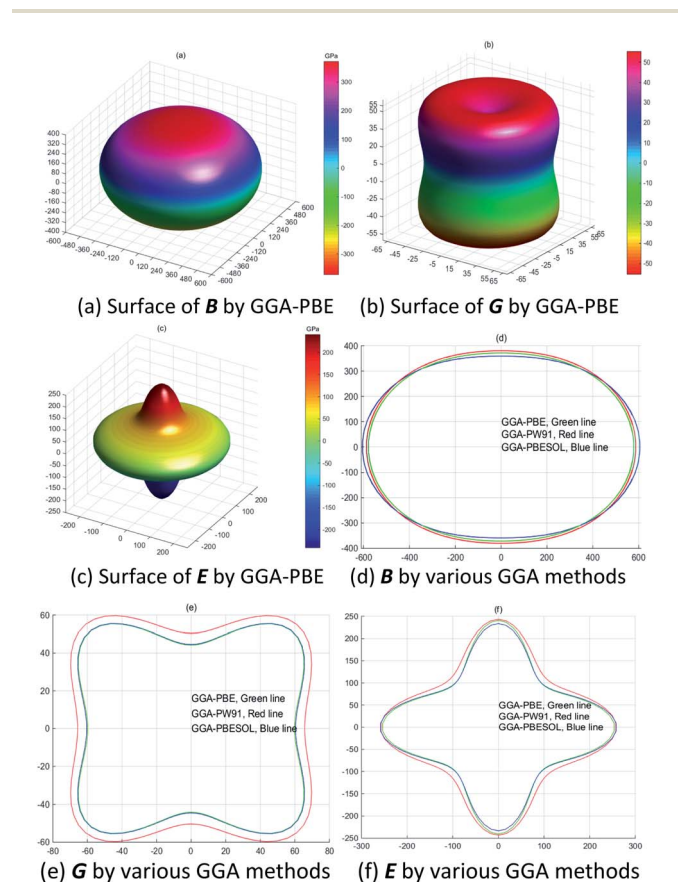

(a) Surface of **B** by GGA-PBE   (b) Surface of **G** by GGA-PBE

(c) Surface of **E** by GGA-PBE   (d) **B** by various GGA methods

(e) **G** by various GGA methods   (f) **E** by various GGA methods

Fig. 6 $LaWN_3$ surface construction of the bulk modulus, shear modulus and Young's modulus.

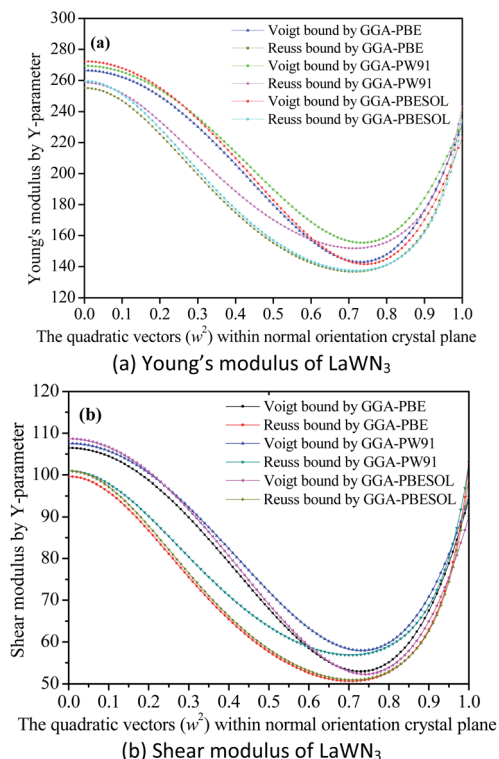(a) Young's modulus of LaWN$_3$

(b) Shear modulus of LaWN$_3$

Fig. 7 Relationship between elastic moduli and plane orientations for LaWN$_3$ by Reuss and Voigt bounds of Y-parameter.

Fig. 6(a–c) show the anisotropy of the bulk modulus, shear modulus and Young's modulus. Meanwhile, the Young's modulus of LaWN$_3$ in Fig. 6(c) has a great deviation in shape from a sphere, indicating that it shows great anisotropy. Fig. 6(d–f) clearly point out the projection curves of the three-dimensional diagrams from Fig. 6(a–c) when the value is zero in the Y-direction and we can see that the various GGA methods (GGA–PBE, GGA–PBESOL and GGA–PW91) have little effect on the curves, with the outer curve being the GGA–PW91 method.

As seen in Fig. 7(a and b), the Young's modulus of LaWN$_3$ using various GGA methods is between 272.23 GPa and 141.58 GPa for the Voigt bounds and between 259.52 GPa and 136.65 GPa for the Reuss bounds as a function of the crystal plane orientation. The maximum value of the Young's modulus is 272.23 GPa and the minimum value is 136.65 GPa. The shear modulus of LaWN$_3$ by Reuss and Voigt bounds of the Y-parameter is between 108.68 GPa and 50.65 GPa, with the Voigt in the region of 52.31–108.68 GPa and the Reuss in the region of 50.65–100.94 GPa. Moreover, in comparison, the Young's modulus and shear modulus of LaWN$_3$ are very close to each other when using various exchange functions (GGA–PBE, GGA–PBESOL and GGA–PW91).

3.5 Optical properties

The reflection spectrum varies with the reflection of electromagnetic wave wavelength characteristics. Materials with different composition or surface structure contribute to the differences in reflection spectrum curves. Light absorption

generally follows Beer–Lambert law, where the absorption coefficient is a constant and the symbol α is the absorption coefficient of the medium to monochromatic light. The energy level and intensity of the absorption peak are related to the imaginary part of the dielectric function. Meanwhile, the absorption coefficient is consistent with the corresponding electron transition probability, which can explain the transition of the electron well.

The optical constants of LaWN$_3$, including conductivity, dielectric constants, absorption spectra, refractive index, loss function and reflectivity, can be calculated by the following equations,

$$n^2 = \frac{\sqrt{\varepsilon_1(\omega) + \varepsilon_2(\omega)}}{2} + \frac{\varepsilon_1(\omega)}{2} \tag{21}$$

$$k^2 = \frac{\sqrt{\varepsilon_1(\omega) + \varepsilon_2(\omega)}}{2} - \frac{\varepsilon_1(\omega)}{2} \tag{22}$$

$$L(\omega) = \frac{\varepsilon_2(\omega)}{\varepsilon_1^2(\omega) + \varepsilon_2^2(\omega)} \tag{23}$$

$$I(\omega) = \sqrt{2}\left[\sqrt{\varepsilon_1^2(\omega) + \varepsilon_1^2(\omega)} - \varepsilon_1(\omega)\right]^{\frac{1}{2}} \tag{24}$$

$$R(\omega) = \left|\frac{\sqrt{\varepsilon_1(\omega) + j\varepsilon_2(\omega)} - 1}{\sqrt{\varepsilon_1(\omega) + j\varepsilon_2(\omega)} + 1}\right|^2 \tag{25}$$

$$\sigma(\omega) = \sigma_1(\omega) + \sigma_2(\omega) = -\frac{i\omega}{4\pi}[\varepsilon(\omega) - 1] \tag{26}$$

where $\varepsilon_1(\omega)$ is the dielectric function, the loss function $L(\omega)$ corresponds to the trailing edge of the reflection spectrum, $n(\omega)$ is the refractive index and $k(\omega)$ represents the extinction coefficient. The loss function $L(\omega)$ describes the loss of energy when electrons pass through the material rapidly. The conductivity function represents the response of a material to an external electric field whose frequency varies with time and refers to the change of conductivity caused by light. The optical properties are usually used to describe the complex dielectric, defined as $\varepsilon(\omega) = \varepsilon_1(\omega) + i\varepsilon_2(\omega)$, which is closely related to the interaction between electrons and photons. The extinction coefficient and refractive index are relative to the imaginary part and the real part, respectively, of the dielectric constant. Thus, we can get the spectrum and band transition of electrons.

Generally, the appearance of peaks in the spectrum can be considered the result of plasma excitation, while the peak position indicates the frequency of the collective excitation of electrons.

The optical constants of LaWN$_3$, including the absorption spectrum, energy-loss spectrum, conductivity, dielectric function, reflectivity, refractive index and extinction coefficient, are calculated and shown in Fig. 8.

It is noted in Fig. 8(a) that there are three absorption regions (0–10.83 eV, 11.59–21.88 eV and 37.9–44.24 eV, respectively), due to the transition from the N-2p state at the top of the valence band to the unoccupied W-5d state at the bottom of the conduction band.
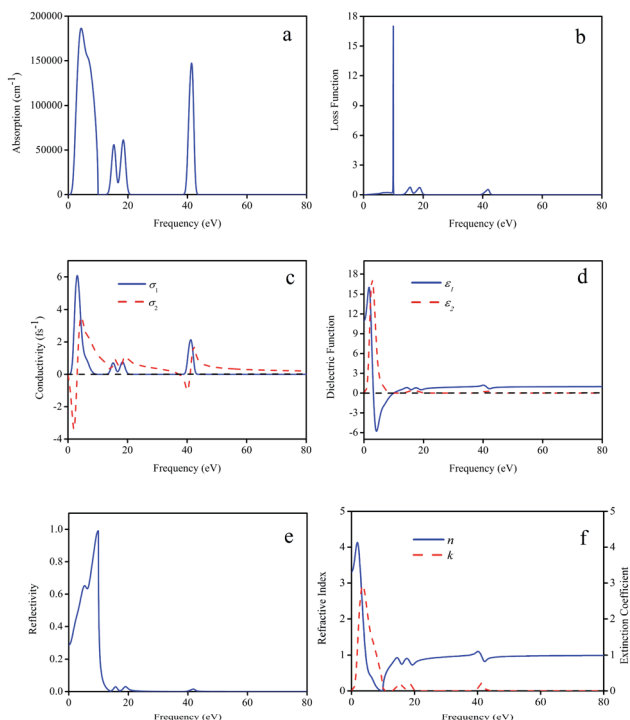
Fig. 8 Calculated optical constants of LaWN$_3$. (a) Absorption spectrum, (b) energy-loss spectrum, (c) conductivity, (d) dielectric function, (e) reflectivity, and (f) refractive index and extinction coefficient.

The peak values of $L(\omega)$ correspond to the trailing edge of the reflection spectrum; 10 eV, 15.6 eV, 18.8 eV and 41.8 eV are the obvious peaks in Fig. 8(b). We can see that the energy loss near 10 eV is larger, while the energy loss in the other region is the smallest. The peak around 10 eV is very steep, indicating that the energy loss is too small, which is very beneficial to reduce loss and improve the storage efficiency. In Fig. 8(c), there are four obvious peaks, among which the strongest peak is located at 3.18 eV with a value of 6.05 fs^{-1} and the other three peaks are located at 15.12 eV, 18.35 eV and 41.21 eV.

As seen in Fig. 8(d), when the frequency is zero, the real part (ε_1) of the dielectric function corresponds to the static dielectric constant and the calculated ε_1 is about 10.98. It can be seen that there are three peaks (2.77 eV, 18.28 eV and 41.27 eV) from the imaginary part of the dielectric function and the strongest peak appears at 2.77 eV with the ε_1 value of 17.14. These differences can be attributed to the N common -2p and W-5d transitions between the conduction band and the valence band.

In Fig. 8(e), as the optical reflection is an important optical loss, the reflection spectrum of LaWN$_3$ is given, in which the positions of some peaks are consistent with the calculations of the energy-loss function. It can be seen that the crystal has high reflectivity in the energy region of 3.17–10 eV. Moreover, Fig. 8(f) shows the refractive index $n(\omega)$ and extinction coefficient $k(\omega)$ and the calculated static refractive index of $n(0)$ is 3.31 at 0 eV. The maximum of the static refractive index is about 4.13 when the frequency is 1.89 eV and the minimum is about 0.75 at 15.23 eV.

In all, it is interesting to find that the spectral characteristics of $n(\omega)$ in Fig. 8(f) are very similar to the dielectric function $\varepsilon_1(\omega)$

in Fig. 8(d), which means that the static dielectric constant $\varepsilon_1(0)$ corresponds to the static refractive index $n(0)$. For the LaWN$_3$ structure, the value of $n(\omega)$ arrives at a maximum value of 4.13 at the energy of 1.89 eV and then decreases gradually to the minimum value of zero at the energy of about 9.87 eV.

In summary, the high conductivities in the low frequency (3.18 eV) and medium frequency (41.21 eV) allow future possible application of LaWN$_3$ in optical materials, such as optical fiber transmission to reduce the loss of light in long-distance transmission due to absorption and scattering. This work is meaningful in the synthesis of nitride perovskites for future application in modern optoelectronics devices.[68,69]

4 Conclusions

Based on DFT, the geometric parameters of LaWN$_3$ were optimized. Then, the elastic constant, band structure, density of states, dielectric constant, refractive index, reflectivity, absorption coefficient and conductivity were calculated and analyzed. The results are as follows:

(1) After geometric optimization with different functional methods, the ABX$_3$-type LaWN$_3$ structure is confirmed to be stable.

(2) From the calculation results of the phonon dispersion spectrum and elasticity criterion, LaWN$_3$ is thermodynamically and mechanically stable.

(3) LaWN$_3$ is an indirect band gap semiconductor ($E_g = 1.181$ eV) and a hybrid orbital is formed near the Fermi level by the contributions of N-2p and W-5d, as well as a small amount of La-5d.

(4) Through study of the elastic properties, LaWN$_3$ produces deformation under stress and shows good ductility.

(5) As for the optical properties of LaWN$_3$, the optical constants, *i.e.*, dielectric constants and refractive index, are higher than those of other ABX$_3$-type materials, which shows that LaWN$_3$ is a very promising functional perovskite material.

The above results provide a theoretical basis to explain the relationship between the electronic structure and physical properties of LaWN$_3$. For further research on LaWN$_3$, surface adsorption, quantum dots, doping, thermodynamics, photocatalysis and piezoelectric properties will be investigated. Investigation of this novel LaWN$_3$ ABX$_3$-type material based on first principles can accelerate the future practical synthesis of the piezoelectric and ferroelectric properties of LaWN$_3$ nitride perovskite using well-established design principles, such as increasing the piezoelectric response in nitride perovskites using morphotropic phase boundaries to better understand the boundary between the polar $R3c$ LaWN$_3$ and non-polar $I4$ LaWO$_x$N$_{3-x}$ structures.[70,71] In all, this investigation helps accelerate the practical synthesis of $R3c$ LaWN$_3$ and improve the efficiency by narrowing the scope of specific chemical reaction conditions.

Conflicts of interest

There are no conflicts to declare.

Acknowledgements

Notes and references

1 J. Hwang, R. R. Rao, L. Giordano, Y. Katayama, Y. Yu and Y. Shao-Horn, *Science*, 2017, **358**, 751–756.

2 H. Najjar and H. Batis, *Catal. Rev.*, 2016, **58**, 371–438.

3 A. Gómez, Q. Wang, A. R. Goñi, M. Campoy-Quiles and A. Abate, *Energy Environ. Sci.*, 2019, **12**, 2537–2547.

4 Y. B. Lu, X. Kong, X. Chen, D. G. Cooke and H. Guo, *Sci. Rep.*, 2017, **7**, 41860.

5 D. Ran, X. Zhang and W. S. Xiao, *Adv. Funct. Mater.*, 2017, **27**, 1702207.

6 X. Zhang, R. Munir, Z. Xu, Y. Liu, H. Tsai, W. Nie, J. Li, T. Niu, D. M. Smilgies, M. G. Kanatzidis, A. D. Mohite, K. Zhao, A. Amassian and S. Liu, *Adv. Mater.*, 2018, **30**, 1707166.

7 M. Kim, G. H. Kim, K. S. Oh, Y. Jo, H. Yoon, K. H. Kim, H. Lee, J. Y. Kim and D. S. Kim, *ACS Nano*, 2017, **11**, 6057–6064.

8 T. Song, X. Cai, M. W.-Y. Tu, X. Zhang, B. Huang, N. P. Wilson, K. L. Seyler, L. Zhu, T. Taniguchi, K. Watanabe, M. A. McGuire, D. H. Cobden, D. Xiao, W. Yao and X. Xu, *Science*, 2018, **360**, 1214–1218.

9 J. Fujioka, T. Okawa, A. Yamamoto and Y. Tokura, *Phys. Rev. B*, 2017, **95**, 121102.

10 L. Glasser, *Inorg. Chem.*, 2017, **56**, 8920–8925.

11 L. Zhang, X. Yang, Q. Jiang, P. Wang, Z. Yin, X. Zhang, H. Tan, Y. M. Yang, M. Wei, B. R. Sutherland, E. H. Sargent and J. You, *Nat. Commun.*, 2017, **8**, 15640.

12 S. Kumar, J. Jagielski, N. Kallikounis, Y.-H. Kim, C. Wolf, F. Jenny, T. Tian, C. J. Hofer, Y.-C. Chiu, W. J. Stark, T.-W. Lee and C.-J. Shih, *Nano Lett.*, 2017, **17**, 5277–5284.

13 H. Tsai, W. Nie, J. C. Blancon, C. C. Stoumpos, C. M. M. Soe, J. Yoo, J. Crochet, S. Tretiak, J. Even, A. Sadhanala, G. Azzellino, R. Brenes, P. M. Ajayan, V. Bulovic, S. D. Stranks, R. H. Friend, M. G. Kanatzidis and A. D. Mohite, *Adv. Mater.*, 2018, **30**, 1704217.

14 F. Jia, K.-B. Siham, B. Fabrice and C. Marilyne, *Composites, Part B*, 2018, **151**, 127–138.

15 H. Chen, F. Ye, W. Tang, J. He, M. Yin, Y. Wang, F. Xie, E. Bi, X. Yang, M. Gratzel and L. Han, *Nature*, 2017, **550**, 92.

16 M. Ans, J. Iqbal, A. I. A. Bhatti and K. Ayub, *RSC Adv.*, 2019, **9**, 34496–34505.

17 N. Raja, D. Murali, S. V. M. Satyanarayana and M. Posselt, *RSC Adv.*, 2019, **9**, 34158–34165.

18 Y. Liu, Q. Xu, S. Chang, Z. Lv, S. Huang, F. Jiang, X. Zhang, G. Yang, X. Tong, S. Hao and Y. Ren, *Phys. Chem. Chem. Phys.*, 2018, **20**, 19950–19957.

19 R. Su, C. Diederichs, J. Wang, T. C. H. Liew, J. Zhao, S. Liu, W. Xu, Z. Chen and Q. Xiong, *Nano Lett.*, 2017, **17**, 3982–3988.

20 C. Tian, T. Guo, S. Zhao, W. Zhai, C. Ge and G. Ran, *RSC Adv.*, 2019, **9**, 35984–35989.

21 Z. Xiao, Q. Wang, X. Wu, Y. Wu, J. Ren, Z. Xiong and X. Yang, *Org. Electron.*, 2020, **77**, 105546.

22 J. Bao and V. G. Hadjiev, *Nano-Micro Lett.*, 2019, **11**, 26.

23 K. Masuko, M. Shigematsu, T. Hashiguchi, D. Fujishima, M. Kai, N. Yoshimura, T. Yamaguchi, Y. Ichihashi, T. Mishima, N. Matsubara, T. Yamanishi, T. Takahama, M. Taguchi, E. Maruyama and S. Okamoto, *IEEE J. Photovolt.*, 2014, **4**, 1433–1435.

24 Y. Kato, S. Fujimoto, M. Kozawa and H. Fujiwara, *Phys. Rev. Appl.*, 2019, **12**, 024039.

25 L. Ba, H. Liu and W. Shen, *Prog. Photovoltaics*, 2018, **26**, 924–933.

26 Y. Wang, H. Arandiyan, H. A. Tahini, J. Scott, X. Tan, H. Dai, J. Gale, A. Rohl, S. C. Smith and R. Amal, *Nat. Commun.*, 2017, **8**, 15553.

27 J. Lu, W. Luo, J. Feng and H. Xiang, *Nano Lett.*, 2017, **18**, 595–601.

28 R. Jacobs, T. Mayeshiba, J. Booske and D. Morgan, *Adv. Energy Mater.*, 2018, **8**, 1702708.

29 S. S. Shin, E. J. Yeom, W. S. Yang, S. Hur, M. G. Kim, J. Im, J. Seo, J. H. Noh and S. I. Seok, *Science*, 2017, **356**, 167–171.

30 M. S. Alkathy and K. C. J. Raju, *J. Alloys Compd.*, 2018, **737**, 464–476.

31 B. Huang and M. Kaviany, *Acta Mater.*, 2010, **58**, 4516–4526.

32 T. Fan, Q.-F. Zeng and S.-Y. Yu, *Acta Phys. Sin.*, 2016, **65**, 118102.

33 M. Ju, J. Dai, L. Ma and X. Zeng, *Adv. Energy Mater.*, 2017, **7**, 1700216.

34 W. Travis, E. N. K. Glover, H. Bronstein, D. O. Scanlon and R. G. Palgrave, *Chem. Sci.*, 2016, **7**, 4548–4556.

35 Y. Fang, C. A. J. Fisher, A. Kuwabara, X. Shen, T. Ogawa, H. Moriwake, R. Huang and C. Duan, *Phys. Rev. B*, 2017, **95**, 014111.

36 M. Ernzerhof and G. E. Scuseria, *J. Chem. Phys.*, 1999, **110**, 5029–5036.

37 P. J. Hasnip, M. I. Probert, K. Refson and M. C. Payne, *Z. Kristallogr. Cryst. Mater.*, 2005, **220**, 567–570.

38 R. Malik, L. Franke and A. Siebes, *Thin Solid Films*, 2001, **381**, 176–182.

39 V. I. Zubov, N. P. Tretiakov, J. N. Teixeira Rabelo and J. F. Sanchez Ortiz, *Phys. Lett. A*, 1994, **194**, 223–227.

40 B. R. Sahu, *Mater. Sci. Eng., B*, 1997, **49**, 74–78.

41 M. G. Brik and C.-G. Ma, *Comput. Mater. Sci.*, 2012, **51**, 380.

42 L. J. Sham and M. Schlüter, *Phys. Rev. Lett.*, 1983, **51**, 1888–1891.

43 P. Mori-Sánchez, A. J. Cohen and W. Yang, *Phys. Rev. Lett.*, 2007, **100**, 146401.

44 S. Sajid, A. M. Elseman, J. Ji, S. Dou, D. Wei, H. Huang, P. Cui, W. Xi, L. Chu, Y. Li, B. Jiang and M. Li, *Nano-Micro Lett.*, 2018, **10**, 51.

45 F. Giustino, *Rev. Mod. Phys.*, 2017, **89**, 015003.

46 D. M. Monahan, L. Guo, J. Lin, L. Dou, P. Yang and G. R. Fleming, *J. Phys. Chem. Lett.*, 2017, **8**, 3211–3215.

47 J. Iles-Smith, D. P. S. Mccutcheon, A. Nazir and J. Mork, *Nat. Photonics*, 2017, **11**, 521–526.

48 I. Niehues, R. Schmidt, M. Drüppel, P. Marauhn, D. Christiansen, M. Selig and R. Bratschitsch, *Nano Lett.*, 2018, **18**, 1751–1757.

49 R. Y. Babkin, K. V. Lamonova, S. M. Orel, Yu. G. Pashkevich and V. F. Meshcheryakov, *Opt. Spectrosc.*, 2012, **112**, 438–442.

50 K. Matsunaga, Y. Iwamoto and H. Matsubara, *J. Mater. Res.*, 2000, **15**, 429–436.

51 S. Tennakoon, Y. Peng, M. Mookherjee, S. Speziale, G. Manthilake, T. Besara, L. Andreu and F. Rivera, *Sci. Rep.*, 2018, **8**, 1372.

52 M. Zhong, Q. Liu, H. Qin, Z. Jiao, F. Zhao, H. Shang, F. Liu and Z. Liu, *Eur. Phys. J. B*, 2017, **90**, 115.

53 X. S. Cao, *J. Low Temp. Phys.*, 2017, **189**, 1–8.

54 C. C. Chen, C. C. Lin, L. G. Liu, S. V. Sinogeikin and J. D. Bass, *Am. Mineral.*, 2001, **86**, 1525–1529.

55 Q. Liu, Z. Liu, L. Feng and H. Tian, *J. Solid State Chem.*, 2012, **196**, 425–434.

56 F. Jia, K.-B. Siham and B. Fabrice, *Mol. Simul.*, 2018, **44**, 285–299.

57 M. Born, K. Huang and M. Lax, *Am. J. Phys.*, 1954, **39**, 113–127.

58 A. Afaq, A. Bakar, S. Anwar, W. Anwar and A. Fazal-e-Aleem, *Int. J. Mod. Phys. B*, 2018, **32**, 1850362.

59 E. Olsson, X. Aparicio-Anglès and N. H. de Leeuw, *J. Chem. Phys.*, 2016, **145**, 224704.

60 J. Fu, F. Bernard and S. Kamali-bernard, *J. Phys. Chem. Solids*, 2017, **101**, 74–89.

61 Y. L. Page, P. Saxe and J. R. Rodgers, *Phys. Status Solidi B*, 2002, **229**, 1155–1161.

62 D. P. Dandekar, *Phys. Rev.*, 1968, **172**, 873–877.

63 R. Terki, H. Feraoun, G. Bertrand and H. Aourag, *Phys. Status Solidi B*, 2005, **242**, 1054–1062.

64 I. R. Shein, K. I. Shein and A. L. Ivanovskii, *J. Nucl. Mater.*, 2007, **361**, 69–77.

65 L. Shi, Y. Duan, X. Yang and L. Qin, *Chin. Phys. Lett.*, 2010, **27**, 159–162.

66 S. F. Pugh, *Philos. Mag.*, 2009, **45**, 823–843.

67 J. Zhang and R. J. Reeder, *Am. Mineral.*, 1999, **84**, 861–870.

68 N. Pandey, A. Kumar and S. Chakrabarti, *RSC Adv.*, 2019, **9**, 29556–29565.

69 F. Hao, C. C. Stoumpos, D. H. Cao, R. P. H. Chang and M. G. Kanatzidis, *Nat. Photonics*, 2017, **8**, 489–494.

70 K. R. Talley, J. Mangum, C. L. Perkins, R. Woods-Robinson, A. Mehta, B. P. Gorman, G. L. Brennecka and A. Zakutayev, *Adv. Electron. Mater.*, 2019, **5**, 1900214.

71 H. Liu, J. Chen, H. B. Huang, L. L. Fan, Y. Ren, Z. Pan, J. X. Deng, L. Q. Chen and X. R. Xing, *Phys. Rev. Lett.*, 2018, **120**, 055501.